

XO-4b: An Extrasolar Planet Transiting an F5V Star

P. R. McCullough¹, Christopher J. Burke¹, Jeff A. Valenti¹, Doug Long¹,
Christopher M. Johns-Krull^{2,3}, P. Machalek^{1,3,4}, K. A. Janes⁵, B. Taylor⁶, J. Gregorio⁷,
C. N. Foote⁸, Bruce L. Gary⁹, M. Fleenor¹⁰, Enrique García-Melendo¹¹, T. Vanmunster¹²

pmcc@stsci.edu

ABSTRACT

We report the discovery of the planet XO-4b, which transits the star XO-4 (GSC 03793-01994, V=10.7, F5V). Transits are 1.0% deep and 4.4 hours in duration. The star XO-4 has a mass of $1.32 \pm 0.02 M_{\odot}$, a radius of $1.55 \pm 0.05 R_{\odot}$, an age of 2.1 ± 0.6 Gyr, a distance of 293 ± 19 pc, an effective temperature of 5700 ± 70 K, a logarithmic iron abundance of -0.04 ± 0.03 relative to solar, a logarithmic surface gravity in cgs units of 4.18 ± 0.07 , and a projected rotational velocity of 8.8 ± 0.5 km s⁻¹. The star XO-4 has periodic radial velocity variations with a semi-amplitude of 163 ± 16 m s⁻¹, due to the planet XO-4b. The planet XO-4b has a mass of $1.72 \pm 0.20 M_{\text{J}}$, a radius of $1.34 \pm 0.048 R_{\text{J}}$, an orbital

¹Space Telescope Science Institute, 3700 San Martin Dr., Baltimore MD 21218

²Dept. of Physics and Astronomy, Rice University, 6100 Main Street, MS-108, Houston, TX 77005

³Visiting Astronomer, McDonald Observatory, which is operated by the University of Texas at Austin.

⁴Department of Physics and Astronomy, Johns Hopkins University, 3400 North Charles Street, Baltimore, MD 21218

⁵Boston University, Astronomy Dept., 725 Commonwealth Ave., Boston, MA 02215

⁶Lowell Observatory, 1400 W. Mars Hill Rd., Flagstaff, AZ 86001

⁷Obs. Atalaia, Alcabideche, Portugal

⁸Vermillion Cliffs Observatory, Kanab, UT

⁹Hereford Arizona Observatory, 5320 E. Calle Manzana, Hereford, AZ 85615

¹⁰Volunteer Observatory, Knoxville, TN

¹¹Esteve Duran Observatory Foundation, Montseny 46, 08553 Seva, Spain

¹²CBA Belgium Observatory, Walhostraat 1A, B-3401 Landen, Belgium

period of 4.12502 ± 0.00002 days, and a heliocentric Julian date at mid-transit of 2454485.9322 ± 0.0004 . We analyze scintillation-limited differential R-band photometry of XO-4b in transit made with a 1.8-m telescope under photometric conditions, yielding photometric precision of 0.6 to 2.0 millimag per one-minute interval. The declination of XO-4 places it within the continuous viewing zone of the Hubble Space Telescope (*HST*), which permits observation without interruption caused by occultation by the Earth. Because the stellar rotation periods of the three hottest stars orbited by transiting gas-giant planets are 2.0, 1.1, and 2.0 times the planetary orbital periods, we note the possibility of resonant interaction.

Subject headings: binaries: eclipsing – planetary systems – stars: individual (GSC 03793-01994) – techniques: photometric – techniques: radial velocities

1. Introduction

During 2007, the number of reported planets that transit stars brighter than $V = 13$ increased markedly from 9 to 23 planets¹. The number of transiting planets reported in the first half of 2008 has already exceeded the total number reported in 2007. This rapid increase in discovery rate is due in part to recently matured search techniques and analysis software applied to thousands of observations of hundreds of thousands of stars by multiple research groups. The planet XO-4b reported here is another in a sequence of discoveries by the XO project (McCullough et al. 2005), facilitated by a collaboration between professional and amateur astronomers.²

The star XO-4 is bright enough to appear in a few all-sky surveys with the following identifiers: GSC 03793-01994 (Morrison et al. 2001), 2MASS J07213317+5816051 (Cutri et al. 2003), and TYC 3793-01994-1 (Høg et al. 2000). For XO-4 the Tycho Catalog reports right ascension $\alpha = 7^{\text{h}}21^{\text{m}}33^{\text{s}}.159 \pm 0.026''$, declination $\delta = +58^{\circ}16'4''98 \pm 0.028''$, and proper motions $\mu_{\alpha} = -18.1 \pm 2.9$ mas yr⁻¹ and $\mu_{\delta} = -4.0 \pm 2.9$ mas yr⁻¹, all for equinox and epoch J2000.

Several recently discovered transiting planets expanded the parameter space of *transiting*

¹Extrasolar Planets Encyclopaedia, <http://exoplanet.eu>

²This paper includes data taken at the Haleakala summit (maintained by the University of Hawaii), Lowell Observatory, McDonald Observatory (operated by the University of Texas at Austin), and numerous backyard observatories.

planets in one way or another at the time of their discovery. For example, GJ 426b (Gillon et al. 2007) is the smallest and least massive transiting planet, and also the only one known to transit an M dwarf. XO-3b (Johns–Krull et al. 2008) is the most massive ($M_p = 12M_J$). HAT-P-2b (Bakos et al. 2007) had the largest eccentricity ($e = 0.52$), until HD 17156b (Barbieri et al. 2007) was discovered with a larger eccentricity ($e = 0.67$) and the longest known period ($P = 21$ days), demonstrating the ephemeral nature of such records. As Harwit (1981) discusses, the limits of the extent of any parameter space begin to show themselves not first in the outliers themselves, but in the “repetitions” of discoveries. Simply put, if nearly every new discovery is unique in some significant way, then clearly we have not yet begun to bound the parameter space. XO-4b is not particularly unusual with respect to other known transiting planets, except perhaps that it orbits a relatively warm star. Only HAT-P-6b (Noyes et al. 2008) and XO-3b orbit slightly warmer stars. In fact, the HAT-P-6 and XO-4 systems are quite similar.

To stimulate additional observations and analysis of the XO-4 system, we report here the characteristics of both the star and the planet. In Section 2 we describe the observations, which include time-series photometry, out-of-transit BVR_CI_C photometry, and spectroscopy with and without iodine absorption lines superposed. In Section 3 we analyze the data and derive the ephemeris of the transits, measure time-dependent radial velocities, and the physical characteristics of the star XO-4, using both its spectrum and its light curve. Section 3.4 applies the numerical models commonly used for transits to scintillation-limited photometry. Section 4 discusses the results and summarizes the conclusions.

2. Observations

2.1. Survey and Extended-Team Photometry

In many ways XO-4 presented an excellent signature of a transiting planet in the XO survey photometry. Figure 1 shows the star is relatively isolated: our automated scripts had estimated that 86% of the flux within the XO cameras’ 75”-radius photometric aperture was due to XO-4. The pixel centroid shifts of XO-4 are consistent with the transit signal being intrinsic to XO-4 rather than the result of a fainter eclipsing stellar binary within the photometric aperture. Making use of the TYCHO-2 and 2MASS catalogs, the 19 mas yr⁻¹ proper motion combined with $V_T=10.85$ and $(V_T-J)=1.19$ places XO-4 on the reduced proper motion diagram of Gould & Morgan (2003) within the $R_\star < 1.25 R_\odot$ cutoff, although by the end of our analysis, we would derive a larger radius. Transits were $\sim 1\%$ deep, flat-bottomed, and steep-edged, all signs of a good candidate for a transiting planet (Figure 2; Table 2). Initially, the 4-hour transit duration from the XO survey data was too long given the initial

G8V spectral type estimate for XO-4 from catalog broad band photometry. However, more accurate photometry and spectroscopy yields an earlier, F5V spectral type and larger R_x , which is consistent with the 4-hour transit duration.

The time line for XO observations covers ~ 100 cycles of XO-4b, which provided an ephemeris sufficiently accurate for follow up photometric observations to recover the transit. The XO survey observed ingresses of five separate transits and egresses of six transits, with only one transit observed in its entirety from ingress to egress. With multiple transits observed and with at least one pair separated by only one cycle, the chance of misidentifying a longer-period orbit with a shorter-period harmonic was small.

Extended Team³ time-series photometry in 2007 November confirmed XO-4 is the variable star, verified and improved the transit’s ephemeris and shape, i.e. depth, duration, and abruptness of ingress and egress. The Extended Team recorded time-series photometry of seven transits; the data are in Table 2. A planetary transit has a nearly achromatic shape; many triple stars do not. The Extended Team observed transits of XO-4b once each in B, V, and I spectral bands and multiple times in R band. The observed shape of the transit is the same in each band, and each observed depth equals the average depth (1.0%) in R band, within the typical uncertainty of 0.1%.

All-sky photometric measurements were made on three dates (2008 January 10, 19 and 20) using a 0.35-meter telescope located in Arizona in B, V, R_c , and I_c bands. Eight Landolt star fields and the XO-4 star field were observed, between airmasses of 1.18 to 1.3. For the B and V bands a total of 54 Landolt stars were observed multiple times per night; for the R_c and I_c bands 33 Landolt stars were observed multiple times. The Landolt field observations provide solutions to the color and airmass terms for each night. Applying the solution to the XO-4 field yields the standard photometry as given in Table 1. The r.m.s. residuals of the Landolt standard stars around the solution provide the uncertainties in photometry.

2.2. Scintillation-limited Photometry with a 1.8-m Telescope

With the Perkins 1.8-m telescope at Lowell Observatory, we obtained R band time series photometry on 2008 January 20 (UT). We obtained five-second CCD exposures at 8-second cadence for six hours of XO-4 and a single comparison star, for a total of 2448 exposures (Figures 3 and 4). Incidentally, these observations with the PRISM instrument of the XO-4b

³The XO Extended Team consists of volunteers who provide photometric follow up of exoplanet candidates as described by McCullough & Burke (2007).

transit followed those made by the same telescope and instrument earlier the same night of a transit of XO-5b (Burke et al. 2008). The PRISM sensor is a cryogenically-cooled Fairchild CCD with 2048 pixels by 2048 pixels, of which we used a 617 pixel by 144 pixel subarray, or $4'.01$ by $0'.94$ at $0''.39$ per pixel, in order to reduce readout times and thereby to increase the fraction of elapsed time collecting photons. The system gain was $2.66 \text{ e}^- \text{ ADU}^{-1}$; the read noise was 7.8 e^- r.m.s., and the detector has been demonstrated to be linear to within $\pm 1\%$ for fewer than 1.0×10^5 electrons pixel^{-1} . The shutter and filters are located near a re-imaged pupil, so any variations from ideal performance will be identical across the focal plane and removed by the differential photometry. The telescope was intentionally de-focused to produce annulus-shaped stellar images in order to reduce the peak irradiance on the CCD detector from the brightest star to $\lesssim 0.8 \times 10^5$ electrons pixel^{-1} per 5-s exposure. The de-focused stellar images gradually increased in diameter from $3''$ to $6''$ as the telescope tracked the star from airmass 1.1 to 2.1. The telescope has an offset guider which maintained the image position to ~ 1 pixel r.m.s. in each axis, throughout the 6 hours of observation, except for 10 minutes during which the images of the stars drifted by 30 pixels (3 diameters of the de-focused stars) and re-stabilized at a new position. The 10-minutes of drifting, from 0.063 to 0.070 days after mid-transit, are indicated by a hash mark at bottom of Figure 3.

A single comparison star, GSC 03793-01990 (labeled “1” in Figure 1), was selected based on its proximity to XO-4 in location, brightness, and color. With respect to XO-4, the comparison star is $3'$ west, 0.21 mag brighter, and 0.04 mag redder in V- R_C color. The photometry appears to be limited by scintillation (Figure 5). In a 5-second exposure at low airmass, the camera collected 3.2 and 4.0 million photons from XO-4 and the comparison star, respectively, implying a Poisson contribution to XO-4’s differential photometric error of 0.9 mmag per exposure. The noise increases with airmass, indicating the Earth’s atmosphere limits the photometric precision. The increase in noise with airmass is predominately due to scintillation ($\propto \text{airmass}^{1.75}$) and marginally due to fewer photons due to the measured extinction of $0.12 \text{ mag airmass}^{-1}$. If we average every seven consecutive exposures into samples with 1-min cadence, the r.m.s. of those samples is 0.6 mmag for exposures near zenith, commensurate with the 1.8 mmag r.m.s. per exposure. In Figure 5 the observed r.m.s. noise is fit well by the solid line, which corresponds to the quadrature sum of Poisson noise from each star and uncorrelated scintillation of each star that is 25% larger than the nominal value given by Dravins et al. (1998, Eq. 10). In the photometric noise model, Poisson and scintillation noise are both $\sim \sqrt{2}$ larger than the noise contribution from a single source since the differential light curve is calculated from the magnitude difference between XO-4 and the comparison star.

2.3. Spectroscopy

On 2007 November 20-21, we obtained cross-dispersed echelle spectra of XO-4 with the 2dcoude spectrometer (Tull et al. 1995) on the 2.7-m Harlan J. Smith (HJS) telescope at McDonald Observatory. Thorium-argon lamp spectra immediately preceding and following each $R=60,000$ stellar spectrum yielded 0.1 km s^{-1} radial velocity precision. The XO-4 observations were at similar zenith distance (34-35 degrees) both nights to improve radial velocity precision. These observations eliminated a stellar or brown dwarf companion in an isolated binary as the cause of the transits, leaving more complex systems (e.g., Mandushev et al. 2005) or a planetary companion as the only plausible explanations. Section 3.3 describes our analysis of the HJS spectra to obtain stellar parameters.

Between 2007 December 21 and 2008 January 15 we obtained cross-dispersed echelle spectra of XO-4 with the high-resolution spectrometer (Tull 1998) on the 11-m Hobby-Eberly Telescope (HET), also located at McDonald Observatory. The $R=63,000$ spectra were obtained through an iodine gas absorption cell to provide an accurate wavelength reference for each observed spectrum. We obtained one spectrum per night for the first two epochs to confirm the planetary signal, and then two spectra per night for the remaining 7 epochs to improve radial velocity precision by $\sqrt{2}$. We processed each echelle spectrum from both telescopes using the optimal extraction procedure described in Hinkle et al. (2000). Section 3.2 describes our analysis of the HET spectra to measure radial velocity variations.

3. Analysis

3.1. Ephemeris

The heliocentric Julian date of minimum light (also mid-transit) is

$$t_{m.l.} = t_c + P \times E, \tag{1}$$

where E is an integer, $t_c = 2454485.9322 \pm 0.0004$ (HJD), and the orbital period, $P = 4.12502 \pm 0.00002$ days. We determine the epoch t_c and its uncertainty using a Monte Carlo method (Section 3.4) of modeling the high-fidelity observations of the transit observed on Jan 20, 2008. We determined the period from t_c and the XO survey observations of two ingresses and two egresses observed 2 years earlier. Due to the 10-minute sampling and $\sim 1\%$ precision of the survey photometry, each ingress or egress has a timing uncertainty of ~ 10 minutes. With four of them observed ~ 180 cycles from t_c , the uncertainty of the period is $\sim 10 \text{ min} / \sqrt{4} / 180 = 0.00002$ days. Although the formal estimate of the period's uncertainty is far smaller than required for any of the analysis reported here, future planning of a time-critical observation,

such as a sequence of spectra to measure the Rossiter effect, one or more years from t_c may benefit from first verifying the ephemeris with additional precision photometry.

3.2. Radial Velocities

We measured XO-4 radial velocities by modeling each HET spectrum (obtained with an I₂ gas absorption cell in the light path) as the product of a shifted stellar template spectrum multiplied by the known absorption spectrum of the I₂ cell and then convolved with the line spread function of the spectrograph. To construct the stellar template, we scaled a high resolution ($\lambda/\Delta\lambda \approx 10^6$) solar spectrum (Wallace, Hinkle, & Livingston 1998) to match the observed line depths in each wavelength interval and then convolved with a rotational broadening kernel that includes the effects of stellar limb-darkening. We obtained an FTS spectrum of the HET I₂ cell (Cochran 2000) from the National Solar Observatory online archive.

For each wavelength interval, the model parameters are a continuum scale factor, an exponent that scales line depth, the iodine wavelength shift, the stellar radial velocity, and slight deviations from a nominal Gaussian line spread function. Using downhill-simplex χ^2 minimization, we adjusted these free parameters to fit ~ 32 separate 1.5 nm wavelength intervals with significant I₂ absorption (521–570 nm). For each observed spectrum, we compute the mean radial velocity and adopt the standard deviation divided by $\sqrt{32}$ as the uncertainty in the mean. The radial velocities, transformed to the barycentric frame of the solar system, are in Table 3 and Figure 6. We phased the radial velocities to the ephemeris of the transits, assumed a circular orbit, and determined the maximum likelihood radial velocity semi-amplitude $K = 163 \pm 16 \text{ m s}^{-1}$.

Precise line bisector measurements (e.g., Torres et al. 2005; Johns–Krull et al. 2008) can be used to detect triple star systems that produce shallow transits that may be misinterpreted as planetary transits. For each of our HET spectra, we measured the mean bisector span of stellar absorption lines free of I₂ and telluric absorption. We find no significant correlation with measured radial velocities, but the significance of this result is limited by the relatively low signal noise ratio of our spectra.

3.3. Stellar Properties from Spectroscopy and Isochrone Analysis

We used the SME package (Valenti & Piskunov 1996) to fit each observed HJS spectrum (Section 2.3) with a synthetic spectrum, adopting the same wavelength intervals (5150–5200

and 6000-6200 Å), line data, atmospheres, and post facto parameter adjustments as Valenti & Fischer (2005). Table 4 lists the resulting stellar parameters for XO-4: effective temperature (T_{eff}), logarithm of the gravity ($\log g$), metallicity ($[M/H]$), projected rotational velocity ($v \sin i$), and logarithm of the abundances of Na, Si, Ti, Fe, and Ni relative to solar ($[Na/H]$, $[Si/H]$, $[Ti/H]$, $[Fe/H]$, and $[Ni/H]$). Our $[M/H]$ parameter is an abundance scale factor for elements other than Na, Si, Ti, Fe, and Ni, so it is not equivalent to standard metallicity. The 1σ uncertainty for each parameter is listed in the “Uncer” column.

We ran the spectroscopic analysis four times, initially allowing $\log g$ to be a free parameter (“Run 1”) and then fixing it at three specific values. Valenti & Fischer (2005) gravities for stars cooler than XO-4 are constrained almost entirely by the collisional damping wings of the Mg I b triplet lines. For stars as warm as XO-4, these damping wings become relatively weak, providing less of a constraint on stellar gravity. Fortunately, the shape of a precise transit light curve provides a strong independent constraint on stellar gravity (e.g., Winn et al. 2008). In Table 4, “Run 3” (in bold) is our preferred solution, as it assumes the value of $\log g$ favored by the transit light curve analysis (Section 3.4). Tabulated results for the other three runs illustrate in a useful format the covariance of stellar parameters, subject to our spectroscopic constraint. Reduced χ^2 for each spectroscopic fit are listed in the χ_r^2 row. SME users should note that Run 1 did not converge to the absolute minimum value χ_r^2 because the Levenberg-Marquardt algorithm used in SME can have some difficulty following shallow valleys in the χ^2 surface that are not aligned with parameter axes.

To obtain stellar mass (M_*), radius (R_*), and age, we interpreted our spectroscopic and photometric results using Yonsei–Yale (Y^2) isochrones (Demarque et al. 2004). We calculated a bolometric correction and interpolated the isochrones using the procedure described in Valenti & Fischer (2005), except that for XO-4 we were forced to assume a sequence of possible distances (180 to 430 pc in steps of 10 pc). Setting the isochrone gravity equal to the gravity used in the SME analysis selects a preferred distance and hence preferred values for stellar mass, radius and age. Figure 7 shows credible parameter intervals for Run 3, which yielded a preferred radius ($1.56R_\odot$) nearly identical to the radius favored by the light curve analysis ($1.55R_\odot$). Using the parameter relationships in Table 4, we can translate the $0.05R_\odot$ uncertainty in R_* (from the light curve analysis) into corresponding uncertainties in distance, stellar gravity, stellar mass, and age. In Table 4 we adopt uncertainties three times these nominal values to account crudely for possible systematic errors in our analysis.

3.4. Light Curve Modeling

In order to determine the physical parameters of the star and the transiting planet (Table 5), we modeled the high-fidelity transit light curve (Figure 3) using the transit model of Mandel & Agol (2002) and the Markov Chain Monte Carlo (MCMC) methodology. Because we used the same MCMC procedure as Burke et al. (2007; 2008), in this paper we describe the assumptions and results but do not describe the MCMC procedure itself. For simplicity, we assume a circular orbit; Section 4 discusses implications of the circular-orbit assumption being invalid.

To fully determine the system parameters from the transit light curve, we adopt an informative prior for $M_\star = 1.34 \pm 0.08 M_\odot$. This initial estimate for M_\star comes from the SME isochrone analysis (§ 3.3). The uncertainty in the prior for M_\star conservatively agrees with the typical uncertainties in M_\star for the homogeneous analysis of other known transiting planets of Torres et al. (2008). Analysis of the transit light curve provides a more precise estimate of $\log g$ than the spectroscopic determination. One iteration of the SME analysis with $\log g$ fixed to this more precise estimate, the resulting variation to M_\star was not significant for our given prior on M_\star . The prior on each of the other parameters, in particular R_\star and R_p , is uniform. The noise in the light curve averages down as expected on one minute times scales thus we assume Gaussian independent noise for the Likelihood function. For the uncertainties associated with each photometric measure of the light curve, we use the analytic model of Poisson noise and scintillation noise (Section 2.2; Figure 5); we note that $\sigma_i = 1.9$ mmag at ingress and $\sigma_e = 4.1$ mmag at egress. The free parameters in the MCMC fit are M_\star , R_\star , $\rho = R_p/R_\star$, τ , t_o , u_1 , u_2 , and zpt , where τ is the total transit duration from 1st to 4th contact, t_o is the transit timing midpoint offset from an initial ephemeris, u_1 and u_2 are the limb darkening coefficients for a quadratic law, and zpt is the flux ratio zero point for the differential light curve.

Table 4 and Table 5 show the resulting parameters for XO-4 and XO-4b, respectively. The median of the MCMC samples provides a robust (hereafter “best”) estimate of each parameter and the uncertainties are the symmetrical confidence interval containing 68% of the samples. The maximum-likelihood model, i.e. in a χ^2 sense, is the solid line in Figure 3, which also shows the data residuals around the maximum-likelihood model.

The best estimate for the limb darkening coefficients ($u_1 = 0.61 \pm 0.1$ and $u_2 = 0.10 \pm 0.23$) are significantly different than the theoretical R-band limb darkening coefficients from Claret et al. (2000) for a star with the properties of XO-4 ($u_1 = 0.24$ and $u_2 = 0.38$). The theoretical B-band limb darkening coefficients ($u_1 = 0.49$ and $u_2 = 0.29$) are closer in agreement to what is measured. To investigate this difference we perform a χ^2 fit to the Perkins transit light curve fixing the limb darkening parameters at their theoretically expected value in the R-

band ($M_\star = 1.32$ also held fixed). The dashed line in Figure 3 shows the resulting transit model. The theoretical limb darkening coefficients result in steeper ingress and egress with a slightly shallower mid transit flux level. In Figure 3, the plot of residuals is with respect to the model with the limb darkening coefficients treated as free parameters in the MCMC analysis, thus the solid line is zero by definition and the dashed line equals the difference due to fixing the limb darkening coefficients at their theoretical values.

Formally, under the assumption of Gaussian independent noise, the theoretical limb darkening coefficients result in $\Delta\chi^2 = 48$ worse fit at $> 6\text{-}\sigma$ for 2 degrees of freedom. To investigate the reliability of these models, we zoom in on the egress portion of the light curve in Figure 4, where the largest amplitude difference between the models occurs and also the largest photometric noise. The smooth solid and dashed lines show the best-fit model with varying and fixed limb darkening coefficients, respectively. The jagged solid line shows binned data to improve the visibility of the light curve. In our data the two most significant excursions from either model are labeled with arrows in Figure 4. We consider two possibilities: either the noise model is correct and we are measuring limb darkening coefficients significantly in conflict with the theoretical ones, or the noise model overestimates the significance of these two excursions of the light curve, causing the limb darkening coefficients to compensate for systematic errors in the light curve. We consider the latter is the case for the excursion near third contact, because during that time, the stars’ positions were shifting on the detector (see § 2.2). On the other hand, other systematic deviations do not correlate with variations in external parameters; an example prior to third contact is indicated also in Figure 3. From analysis of ground-based and space-based light curves, Southworth (2008) concludes that if limb-darkening coefficients are not included as fitted parameters, uncertainties in other parameters may be underestimated, because the highest-quality light curves (e.g. spectrophotometric, space-based observations of HD 209458b) show significant differences between theoretically-predicted and observationally-derived limb-darkening coefficients. We concur with Southworth (2008) that multiple observations may be useful to discern limitations of a single light curve. The choice of limb darkening profile does not significantly affect R_\star or the planetary properties in the case of XO-4b. The difference in parameters, $\Delta R_\star = 0.07 \pm 0.05 R_\odot$, $\Delta\rho = -0.0017 \pm 0.0013$, $\Delta R_p = 0.03 \pm 0.05 R_J$, $\Delta t_o = 0.4 \pm 0.6$ mn, are in the sense of MCMC analysis minus fixed limb darkening coefficients and the uncertainty is the uncertainty in the parameter from the MCMC analysis only.

4. Discussion and Conclusion

Table 6 compares physical characteristics of XO-4 and two similar transiting systems, HAT-P-4 (Kovacs et al. 2007) and HAT-P-6 (Noyes et al. 2008). The HAT systems were selected for comparison because their stars are similar to XO-4. The relatively large duty cycles of the transits of all three planets imply low mean densities for the host stars, a fact confirmed by the SME analysis of their spectra. The three planets radii are similar but their masses differ by as much as a factor of 2.5.

The mass of XO-4b ($1.72 M_J$) places it at the the margin of the bulk of the distribution of planetary masses for planets with orbital periods between 3 and 5 days. For such planets, the distribution declines rapidly with mass for $M_p \gtrsim 1 M_J$, and the upper $\sim 10\%$ of the distribution of gas giants (4 of ~ 40 reported) is spread broadly over the range from 1 to 12 M_J . The latter approximate description is true for both the set of planets that transit, for which the mass is known, and the set of planets that do not, for which a minimum mass is known. The two sets are similar in number, ~ 20 planets each. That the distribution has a sharp decline at $\sim 1 M_J$ (or between 1 and 2 M_J) is convincing, but the shape of the tail of the distribution for $M_p \gtrsim 1 M_J$ is poorly determined for this period range, due to the small number of planets. XO-4b increases that small number by one.

Analysis of transiting systems yields orbital inclinations and stellar radii. These quantities may be combined with $v \sin i$ to estimate stellar rotation periods,

$$P_* = \frac{2\pi\phi R_*}{v \sin i}, \quad (2)$$

where ϕ is a factor of order unity that accounts for differential rotation and any systematic errors in $v \sin i$. SME yielded $v \sin i = 1.7 \text{ km s}^{-1}$ for the Sun (Valenti & Piskunov 1995), which rotates every 24 days at the equator and every 30 days at the pole. Adopting 27 days as the characteristic rotation period of the Sun implies $\phi = 0.91$. With this value of ϕ , the rotation periods of the three warmest stars known to host transiting planets are 8.1, 3.4, 7.7 days for XO-4, XO-3, and HAT-P-6, respectively. Adopting $R_* = 1.38 R_\odot$ from Winn et al. (2008) for XO-3, these stellar rotation periods are 2.0, 1.1, and 2.0 times the planetary orbital periods. XO-3b is massive enough that the star (or at least the convective envelope) may have been forced into synchronous rotation. XO-4b and HAT-P-6b have orbital periods that are twice the stellar rotation period, suggesting that their orbits may be affected by resonant interactions with their rotating host stars. On the other hand, planets (e.g., HAT-P-2b and HAT-P-7b) orbiting slightly cooler stars do not have orbital periods that are small multiples of the stellar rotation period. Perhaps Jupiter mass planets are only able to interact effectively with stars that have very shallow surface convection zones. The discovery of additional planets that transit warm F dwarfs will test whether resonant

interactions can affect planetary orbital periods or stellar rotation periods. One issue to keep in mind, however, is a possible selection effect against stars with large $v \sin i$ because broad lines make difficult measuring radial velocity variations and the process of discriminating planets from triple star systems.

We emphasize that this analysis assumed the orbit of XO-4b is circular, i.e. $e = 0$. If that assumption is false, i.e. $e > 0$, logically the conclusions are invalid and all the derived physical parameters will change accordingly. The planetary mass is proportional to $K \sqrt{1 - e^2}$ (Hilditch 2001; Equation 2.53), so only an eccentricity $\gtrsim 0.5$ would change the planetary mass estimate significantly compared to its fractional uncertainty ($\sim 10\%$). From the measured depth of the transit, the planetary radius is proportional to the stellar radius, and the latter is proportional to the transverse velocity of the planet at transit. The latter velocity depends on the argument of periastron but is bound by its values at periastron and apastron, i.e. $1 \pm e$ times its value for a circular orbit of the same period. Hence an eccentricity $e \gtrsim 0.035$ could change the planetary radius estimate by $\gtrsim 1\text{-}\sigma$. Interestingly, the *amplitudes* of the radial velocity curve and the light curve readily reveal the *ratios* of planetary-to-stellar masses and radii, but the detailed *shapes* of both curves are required to measure precisely the radii distinctly.

In addition to assuming $e = 0$, one might also assume that the impact parameter $b = 0$, i.e. that the planet’s path crosses the center of the star. Although there is no physical justification for such an assumption, it can be helpful in bounding the limits of the derived physical parameters. If both $e = 0$ and $b = 0$, the density of the star $\rho_*(e = 0; b = 0)$ is determined by the orbital period and the duration of the transit. In that case, the derived radius of the star $R_*(e = 0; b = 0)$ is simply proportional to $M_*^{-1/3}$, where the mass of the star, M_* is estimated from the spectra and the isochrone analysis. The density $\rho_*(e = 0; b = 0)$ is an upper limit, i.e. $\rho_*(e = 0; b = 0) \geq \rho_*(e = 0; b \geq 0)$.

The scintillation-limited, high-cadence photometry of XO-4 presented here has a small r.m.s. per unit time, $0.6 \text{ mmag min}^{-1}$, at small airmass and during planetary ingress, but which increases with airmass to $\gtrsim 2 \text{ mmag min}^{-1}$ at airmass $\gtrsim 2$, during planetary egress. To improve confidence in the parameters derived for the XO-4 system, additional high-fidelity time-series photometry would be beneficial. Observations above the Earth’s atmosphere are not limited by scintillation and can more nearly achieve Poisson-limited results, which for XO-4 with a comparable spectral band and optical throughput, would be $\sim 0.2 \text{ mmag min}^{-1}$ if operational overheads can be made negligible. The declination of XO-4 places it within the continuous viewing zone of the Hubble Space Telescope (*HST*), which permits observation without interruption caused by occultation by the Earth. The latter circumstance may enhance XO-4’s potential for precision spectrophotometry, because those

gaps and issues associated with them potentially may cause systematic errors in precision time series obtained with *HST*.

We thank the staff of the University of Hawaii, Institute for Astronomy, Haleakala Observatories. We especially thank J. Heasley, M. Maberry, and R. Ratkowski for assistance in operations on Maui. We thank the staffs of McDonald Observatory and Lowell Observatory.

R. Bissinger, P. Howell, F. Mallia, G. Masi, K. Richardson, J. G., C. N. F., B. L. G., M. F., E. G.-M., and T. M. observe for the XO Extended Team. Radek Poleski assisted with extrasolar planet candidate identification. Lisa Prato and Naved Mahmud assisted with observing at McDonald Observatory. D. Bell transmitted HET data to us.

This research made use of the Royal Beowulf cluster at STScI; the SIMBAD database, operated at CDS, Strasbourg, France; data products from the Two Micron All Sky Survey (2MASS), the Digitized Sky Survey (DSS), and The Amateur Sky Survey (TASS); source code for transit light-curves (Mandel & Agol 2002); and community access to the HET. XO is funded primarily by NASA Origins of Solar Systems grant NNG06GG92G, with additional funding from the STScI Director's Discretionary Fund.

REFERENCES

- Bakos, G. Á., et al. 2007, *ApJ*, 670, 826
- Barbieri, M., et al. 2007, *A&A*, 476, L13
- Burke, Christopher J., et al. 2007, *ApJ*, 671, 2115
- Burke, Christopher J., et al. 2008, *ApJ*, submitted
- Claret, A. 2000, *A&A*, 363, 1081
- Cochran, W. 2000, FTS spectrum of I2 Cell HRS3 at 69.9 C.,
ftp://nsokp.nso.edu/FTS_cdrom/FTS50/001023R0.004
- Cutri, R. M., et al. 2003, The IRSA 2MASS All-Sky Point Source Catalog, NASA/IPAC Infrared Science Archive
- Demarque, P., Woo, J-H, Kim, Y-C, & Yi, S. K. 2004, *ApJS*, 155, 667
- Dravins, D., Lindegren, L., Mezey, E. & Young, A. T. 1998, *PASP*, 110, 610

- Fischer, D. A., & Valenti, J. 2005, *ApJ*, 622, 1102
- Gillon, M., et al. 2007, *A&A*, 472, L13
- Harwit, M. 1981, *Cosmic discovery. The search, scope, and heritage of astronomy*, Brighton: Harvester Press
- Høg, E., et al. 2000, *A&A*, 355, L27
- Hinkle, K., Wallace, L., Valenti, J., & Harmer, D. 2000, *Visible and Near Infrared Atlas of the Arcturus Spectrum 3727-9300 Å*, ed. Kenneth Hinkle, Lloyd Wallace, Jeff Valenti, and Dianne Harmer. (San Francisco: ASP) ISBN: 1-58381-037-4, 2000
- Johns-Krull, C. M., et al. 2008, *ApJ*, 677, 657
- Kovács, G., et al. 2007, *ApJ*, 670, L41
- Mandel, K., & Agol, E. 2002, *ApJ*, 580, L171
- Mandushev, G., et al. 2005, *ApJ*, 621, 1061
- McCullough, P. R. & Burke, C. J. 2007, *Astronomical Society of the Pacific Conference Series*, 366, 70
- McCullough, P. R., Stys, J. E., Valenti, J. A., Fleming, S. W., Janes, K. A., & Heasley, J. N. 2005, *PASP*, 117, 783
- Gould, A., & Morgan, C. W. 2003, *ApJ*, 585, 1056
- Morrison, J. E., Röser, S., McLean, B., Bucciarelli, B., & Lasker, B. 2001, *AJ*, 121, 1752
- Southworth, J. 2008, *MNRAS*, 444
- Torres, G., Konacki, M., Sasselov, D. D., & Jha, S. 2005, *ApJ*, 619, 558
- Torres, G., Winn, J. N., & Holman, M. J. 2008, *ApJ*, 677, 1324
- Tull, R. G. 1998, *Proc. SPIE*, 3355, 387
- Tull, R. G., MacQueen, P. J., Sneden, C., & Lambert, D. L. 1995, *PASP*, 107, 251
- Valenti, J. A., & Fischer, D. A. 2005, *ApJS*, 159, 141
- Valenti, J. A., & Piskunov, N. 1996, *A&AS*, 118, 595

Wallace, L., Hinkle, K., & Livingston, W. 1998, An atlas of the spectrum of the solar photosphere from 13,500 to 28,000 cm^{-1} (3570 to 7405 \AA), Publisher: Tucson, AZ: National Optical Astronomy Observatories

Winn, J. N., et al. 2008, ArXiv e-prints, 804, arXiv:0804.4475

Table 1. Photometry

Star ^a	B	V	R _C	I _C	V-R _C
XO-4	11.240	10.674	10.324	10.057	0.350
1	11.217	10.503	10.109	9.758	0.394
2	11.853	10.329	9.482	8.748	0.847
3	12.030	11.613	11.358	11.084	0.255
4	13.185	12.526	12.184	11.798	0.342
5	13.018	12.314	11.938	11.560	0.376
6	12.555	11.475	10.904	10.390	0.571
7	13.828	13.121	12.663	12.297	0.458
8	14.358	13.787	13.408	13.073	0.378
9	14.833	13.930	13.362	12.834	0.568

^aStars are identified in Figure 1. The $1\text{-}\sigma$ uncertainties are 0.029, 0.019, 0.008, and 0.023 mag for B, V, R_C, and I_C respectively. The 2MASS magnitudes for XO-4 are 9.667, 9.476, 9.406 for J, H, and K_s respectively (Skrutskie et al. 2006).

Table 2. Time-Series Photometry^a

HJD	Brightness [mag]	Uncertainty ($1\text{-}\sigma$) [mag]	Filter ^b	N ^c	Observer ^d
2453691.10864	0.0005	0.0096	W	1	XO
2453691.10889	-0.0052	0.0088	W	1	XO
2453691.11645	0.0087	0.0095	W	1	XO
2453691.11597	-0.0043	0.0088	W	1	XO
2453691.12256	-0.0032	0.0094	W	1	XO

^aThe entire table is in the electronic edition. The printed edition contains only a sample to establish the format.

^bStandard filters, except W = wide, 400-700 nm.

^cAverage of N measurements.

^dObserver initials, except XO is the XO cameras.

Table 3. Radial Velocity Shifts

Julian Date	Radial Velocity Shift [m s ⁻¹]	Uncertainty (1 σ) [m s ⁻¹]
2454455.7622	257	57
2454457.7597	-127	40
2454469.9042	-88	43
2454474.6989	-166	31
2454476.8855	140	39
2454477.8677	-53	39
2454479.8429	-34	46
2454480.6910	172	47
2454480.8856	141	39

Table 4. Stellar Properties of XO-4

Parameter	Run 1	Run 2	Run 3	Run 4	Uncer
<i>Spectroscopic Analysis:</i>					
T_{eff} (K)	6249	6349	6397	6491	70
$\log g$ (cgs)	3.98	4.09 ^a	4.18^a	4.30 ^a	0.07 ^b
[M/H]	-0.05	-0.02	-0.02	0.03	0.05
$v \sin i$ (km s ⁻¹)	9.0	8.7	8.8	8.5	0.5
[Na/H]	-0.12	-0.05	-0.02	0.07	0.2
[Si/H]	-0.02	0.01	0.03	0.04	0.02
[Ti/H]	-0.01	0.00	-0.02	0.02	0.07
[Fe/H]	-0.09	-0.08	-0.04	-0.03	0.03
[Ni/H]	-0.21	-0.04	-0.02	0.05	0.05
χ_r^2	1.82	1.77	1.77	1.81	...
<i>Isochrone Analysis:</i>					
d (pc)	343	312	293	257	19 ^b
M_*/M_\odot	1.34	1.33	1.32	1.29	0.02 ^b
R_*/R_\odot	1.96	1.76	1.56	1.33	0.05 ^c
Age (Gyr)	3.5	2.9	2.1	1.3	0.6 ^b

^aValue of $\log g$ was fixed during the SME analysis.

^bThree times the uncertainty obtained by propagating $0.05R_\odot$ uncertainty in R_* .

^cUncertainty from light curve analysis.

Table 5. The Planet XO-4b

Parameter	Value ^a	Notes
P	4.12502 ± 0.00002 d	Period
t_c	2454485.9322 ± 0.0004 HJD	Transit midpoint
e (assumed)	0	Eccentricity
K	163 ± 16 m s ⁻¹	
M_p	1.72 ± 0.20 M_J	Mass
R_p	1.34 ± 0.048 R_J	Radius
a	0.0555 ± 0.0011 A.U.	Semi-major axis
a/R_*	7.7 ± 0.2	
R_p/R_*	0.089 ± 0.001	
i	88.7 ± 1.1 deg	Inclination
b	0.18 ± 0.14	Impact parameter

^a $R_J = 71492$ km; $M_J = 1.8988e27$ kg

Table 6. Comparison of Three Transiting Systems^a

Parameter	HAT-P-4	HAT-P-6	XO-4	Uncer ^b
<i>Stars:</i>				
T_{eff} (K)	5860	6570	6397	70
$\log g$ (cgs)	4.14	4.22	4.18	0.07
$v \sin i$ (km s ⁻¹)	5.5	8.7	8.8	0.5
[Fe/H]	+0.24	-0.13	-0.04	0.03
Distance, (pc)	310	260	293	19
Mass, (M_{\odot})	1.26	1.29	1.32	0.02
Radius, (R_{\odot})	1.59	1.46	1.56	0.05
Age (Gyr)	4.2	2.3	2.1	0.6
<i>Planets:</i>				
Period (d)	3.06 ^c	3.85 ^c	4.13 ^c	n/a ^c
Mass (M_{J})	0.68	1.06 ^c	1.72	0.20
Radius (R_{J})	1.27	1.33	1.34	0.048

^aHAT-P-4 (Kovacs et al. 2007); HAT-P-6 (Noyes et al. 2008); XO-4 (this work).

^bUncertainty is for XO-4; those for HAT-P-4 and HAT-P-6 are similar or smaller.

^cTabulated value has been rounded.

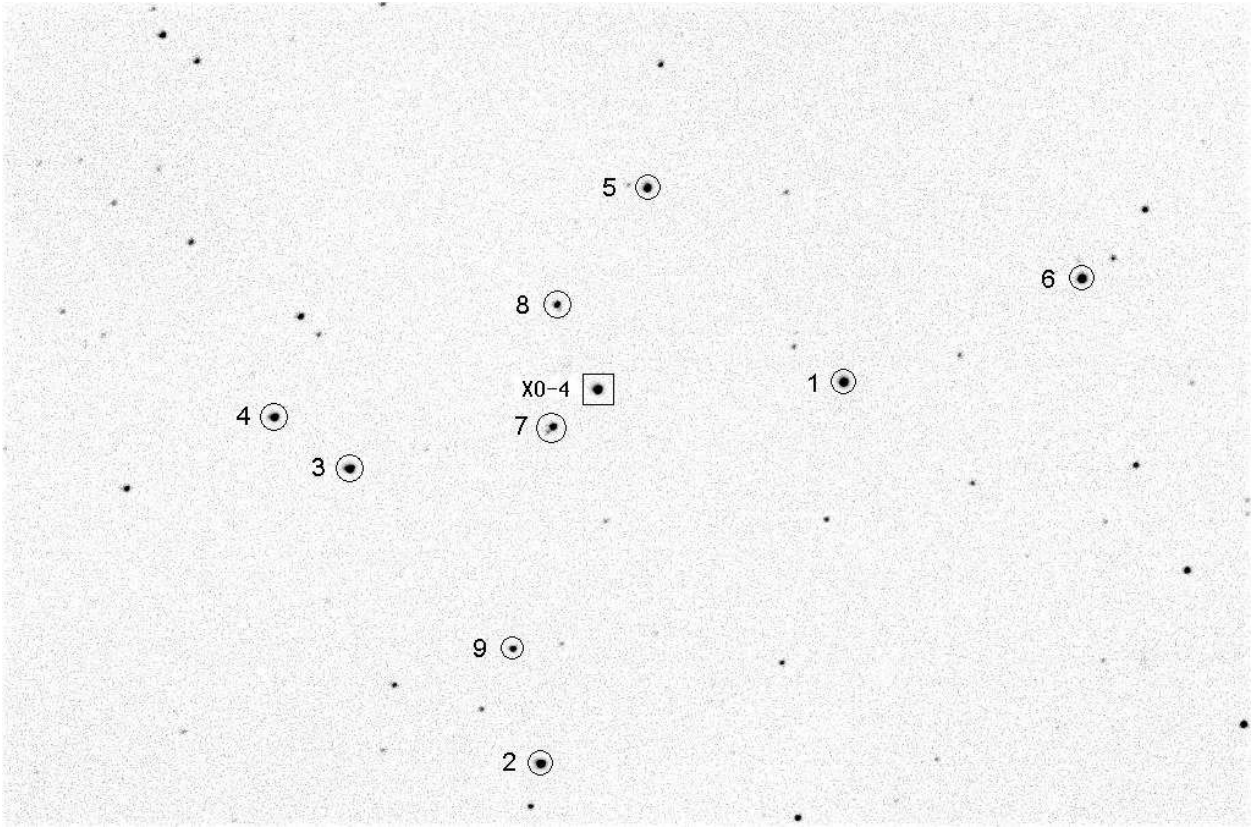


Fig. 1.— X0-4 is inside the square. Stars from Table 1 are circled and numbered. The CCD image is 16' by 11' with North up and East to the left.

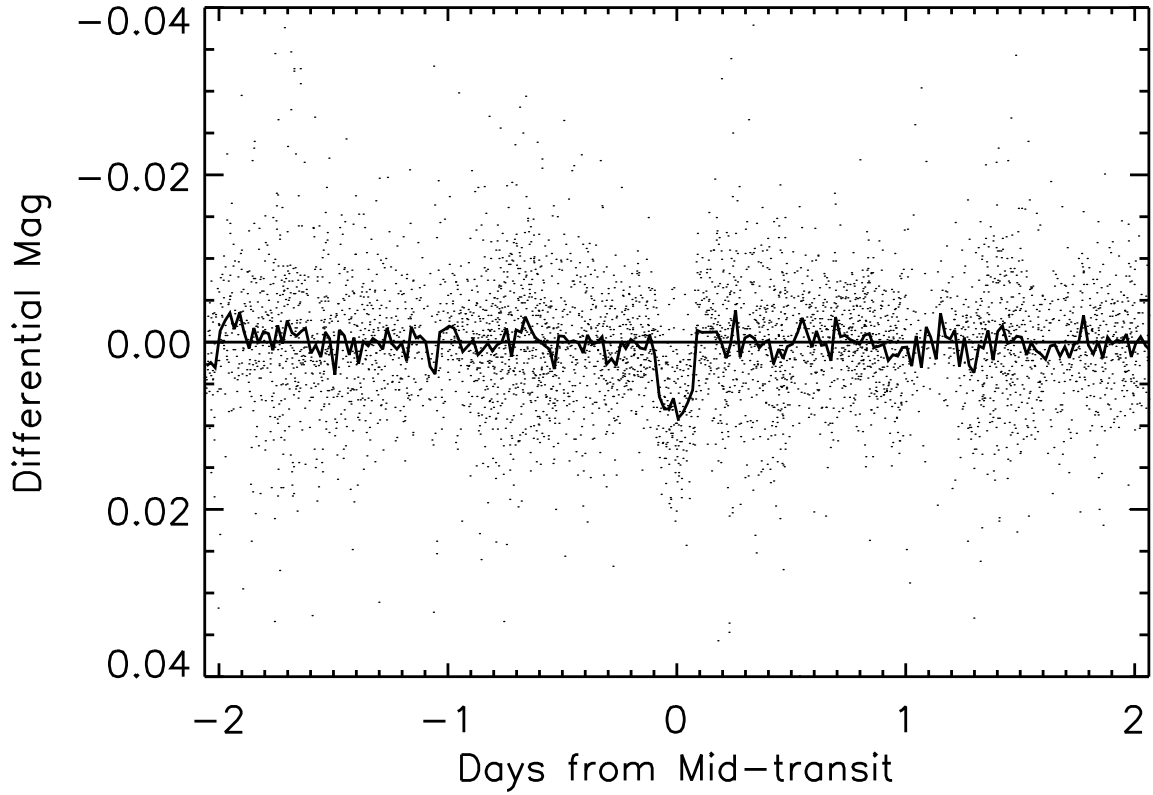


Fig. 2.— Photometry of XO-4 by the two XO cameras over two seasons from Nov 2005 to Mar 2007 are shown wrapped and phased according to the ephemeris of Equation 1 and averaged in 30-minute bins (line).

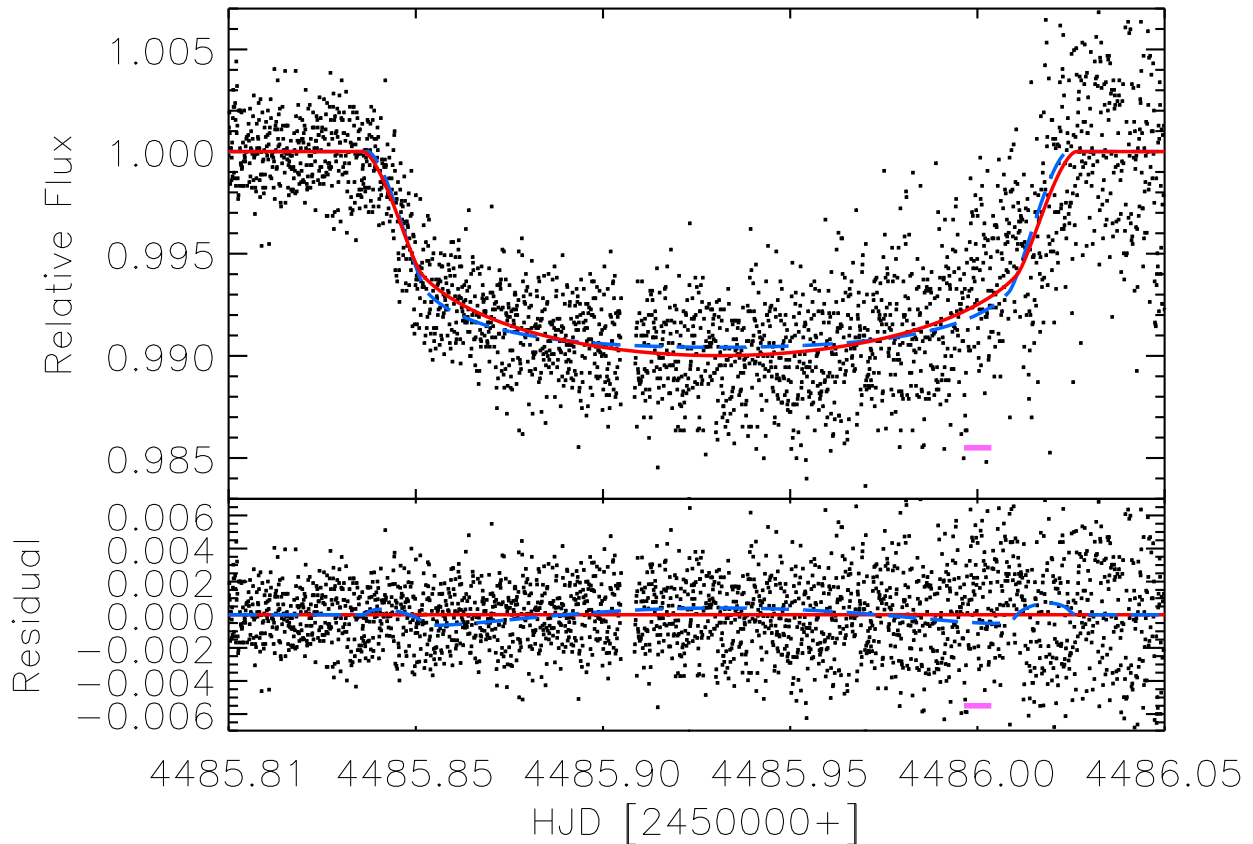


Fig. 3.— *Top*: Time-series R-band photometry of XO-4 as observed with the Lowell 1.8-m Perkins telescope and PRISM camera during the Jan 20, 2008 transit of XO-4b. The data (2448 points), the best-fitting model in a χ^2 sense from the MCMC analysis (solid line), and the best-fitting model in a χ^2 sense with limb darkening coefficients fixed at the R-band theoretical values of Claret (2000) (dashed line). *Bottom*: Residual from the best-fit model from the MCMC analysis (points) and difference between models with variable and fixed to the theoretical limb darkening coefficients (dashed line).

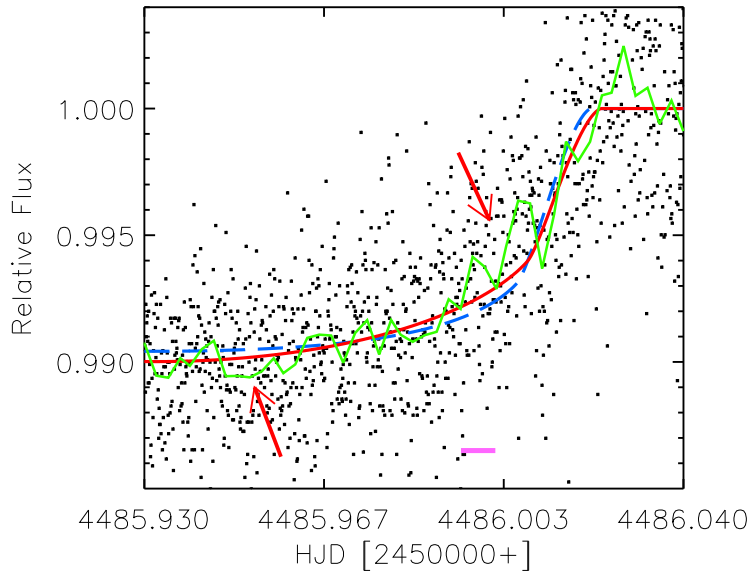
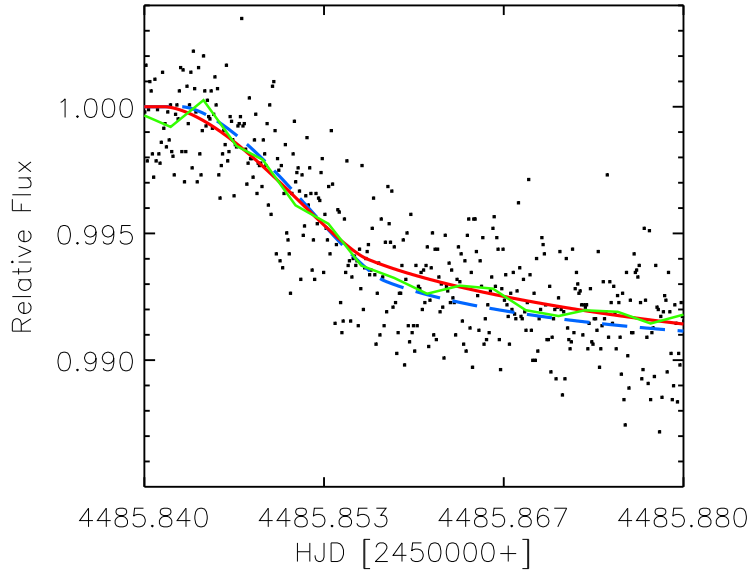


Fig. 4.— Detail of ingress (upper) and egress (lower) of the Lowell 1.8-m Perkins light curve (points) along with data in bins (jagged solid line). Best-fitting transit model in a χ^2 sense from the MCMC analysis with limb darkening coefficients as free parameters (smooth solid line). Best-fitting transit model in a χ^2 sense with limb darkening coefficients fixed at the

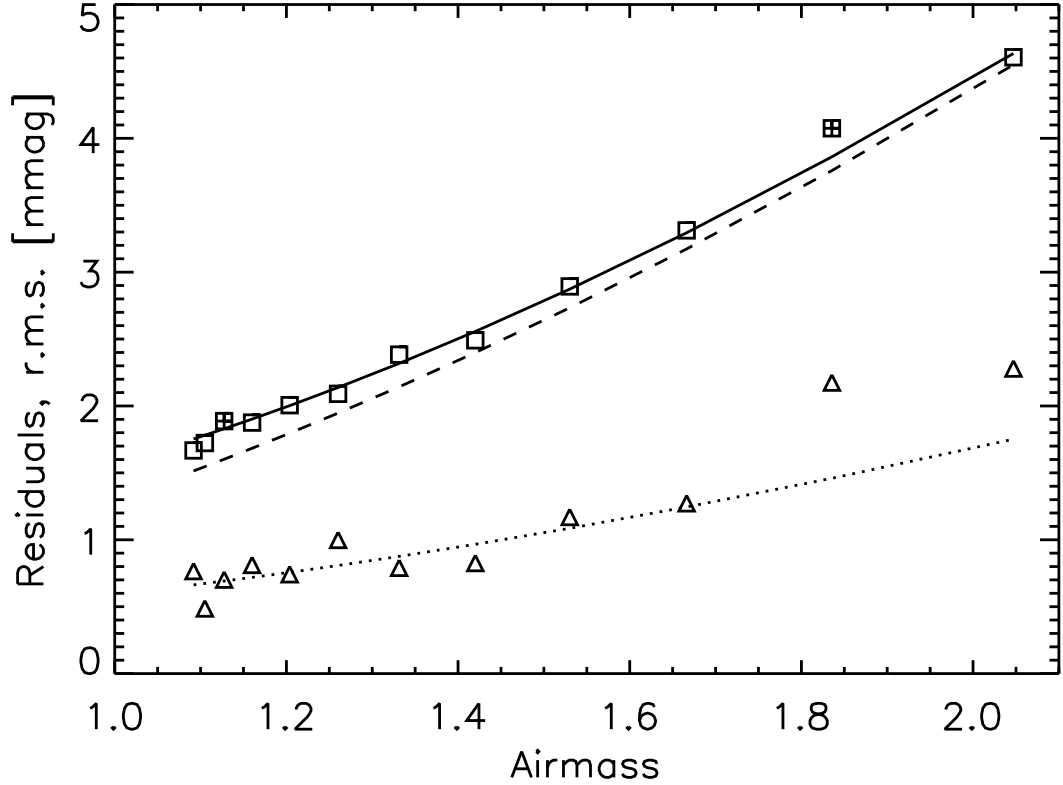


Fig. 5.— Scintillation-limited photometry with the Perkins 1.8-m telescope in R band. The data (squares) are the standard deviations of ~ 225 samples within each of twelve 30-minute intervals of differential photometry of the star XO-4 after a best-fit model to the transit of XO-4b was subtracted. Data at the moments of ingress and egress are indicated by + symbols within the squares at airmasses 1.13 and 1.84, respectively. The solid line is the quadrature sum of contributions from scintillation (dashed line) and Poisson noise (0.9 mmag per 5-sec exposure). The dashed line is proportional to the airmass raised to the power 1.75, as expected for scintillation (see text). The triangles are the same data averaged in 1-minute intervals, with 7 samples per minute. The dotted line is $\sqrt{7}$ times less than the solid line.

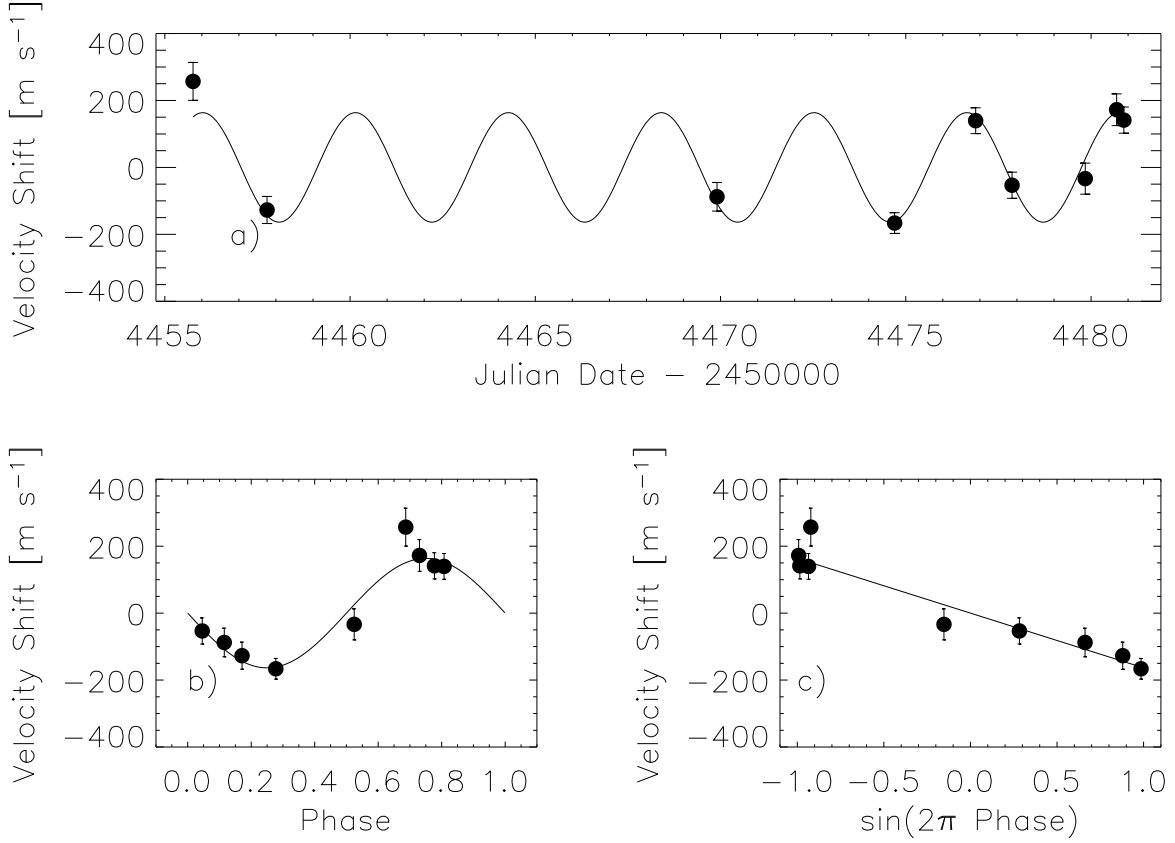


Fig. 6.— a) The radial velocity of XO-4 oscillates sinusoidally with a semi-amplitude $K = 163 \pm 16 \text{ m s}^{-1}$. b) The period and phase of the radial velocities were fixed at values determined by the transits. The mean stellar radial velocity with respect to the solar system’s barycenter has been subtracted. c) In this representation of the data, a circular orbit yields a straight line of slope $-K$.

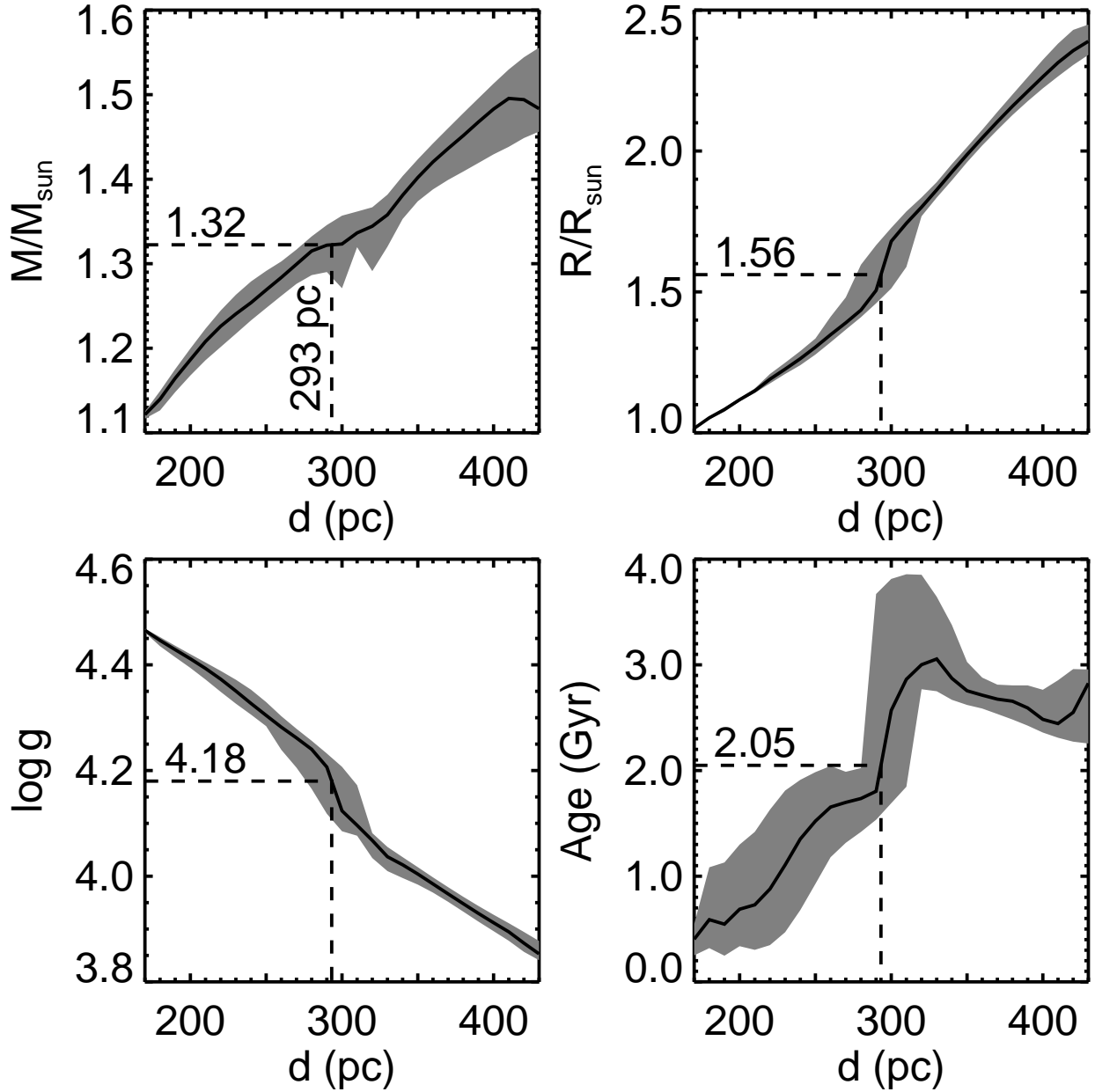


Fig. 7.— Credible intervals for XO-4 stellar properties as a function of assumed distance, based on the “Run 3” isochrone analysis with $\log g = 4.18$ from the light curve analysis.